Supporting Information

Enhanced Oxygen Electrode Kinetics at Low Temperatures: Infiltrated $Sr(Ti_{0.3}Fe_{0.55}Co_{0.15})O_{3-\delta}$–$La_{0.8}Sr_{0.2}Ga_{0.8}Mg_{0.2}O_{3-\delta}$ Nanocomposite for Solid Oxide Cells

Dong-Yeon Kim [†], Ju-Ho Shin [†], Hae-In Jeong [†], Beom-Kyeong Park [*]

Department of Materials Science and Engineering, Pusan National University, Busandaehak-ro 63beon-gil 2, Geumjeong-gu, Busan 46241, Republic of Korea

*** Corresponding author**

E-mail: b-park@pusan.ac.kr

[†] These authors contributed equally.

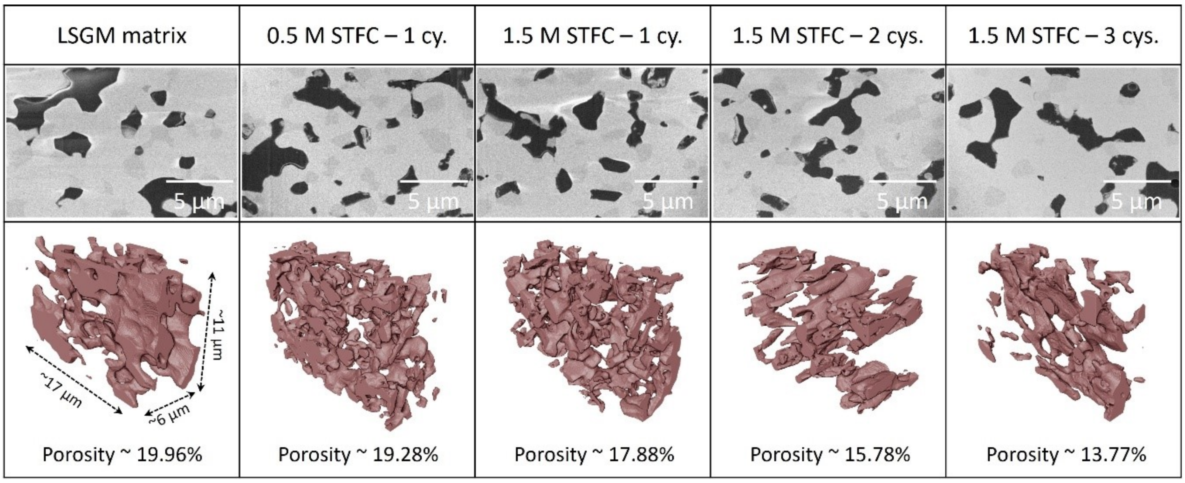

Figure S1. Representative FIB–SEM images (solid = gray; pore = black) and reconstructed 3D pore structures for porous LSGM matrix and those treated with 0.5 M STFC 1 cycle, 1.5 M STFC 1 cycle, 1.5 M STFC 2 cycles, and 1.5 M STFC 3 cycles.

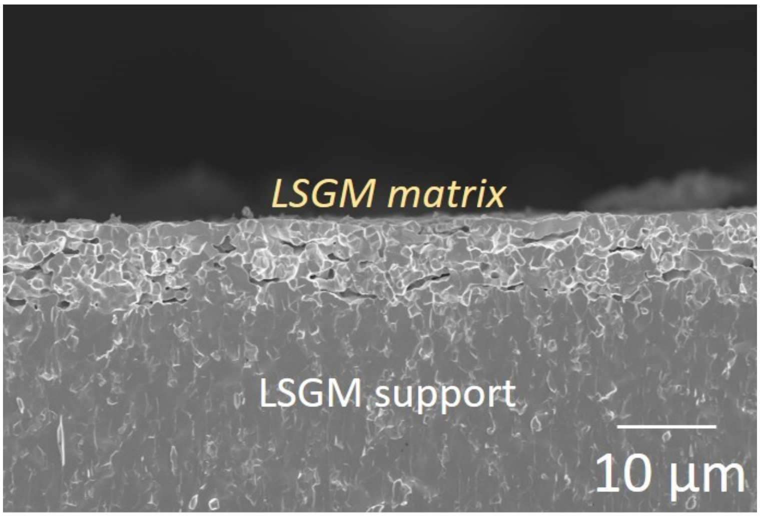

Figure S2. Cross-sectional SEM image of a porous LSGM matrix on an LSGM electrolyte support.

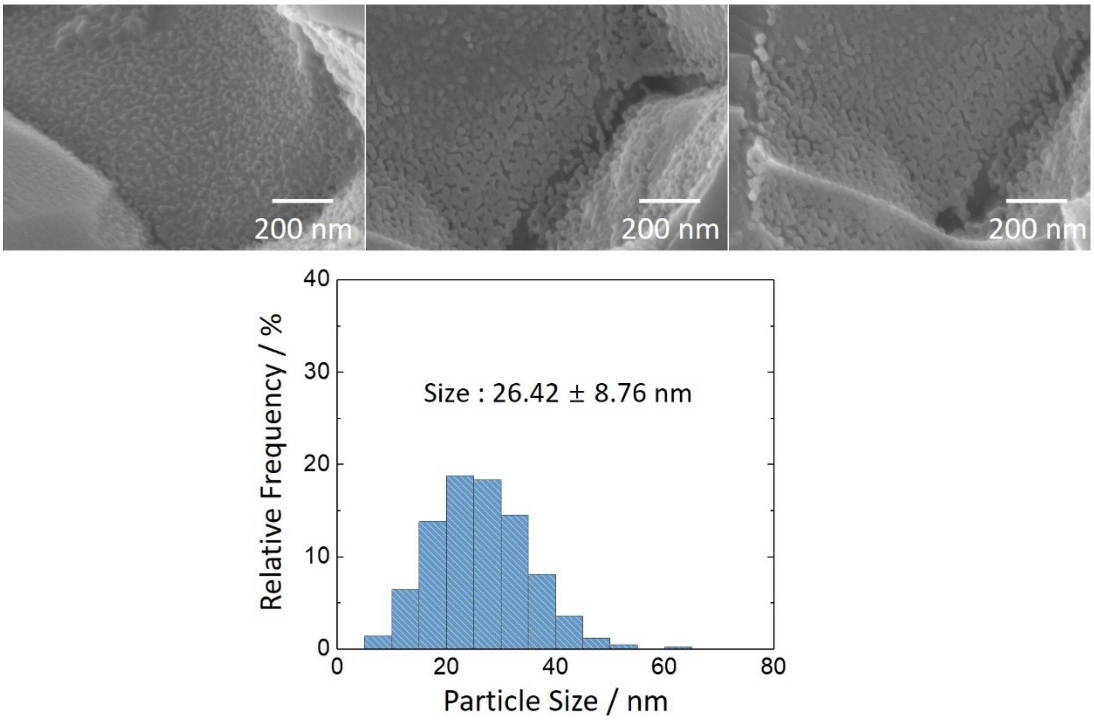

Figure S3. High-magnification SEM images of the STFC (~4.2 vol%)–LSGM electrode, with an STFC particle size distribution analysis result.

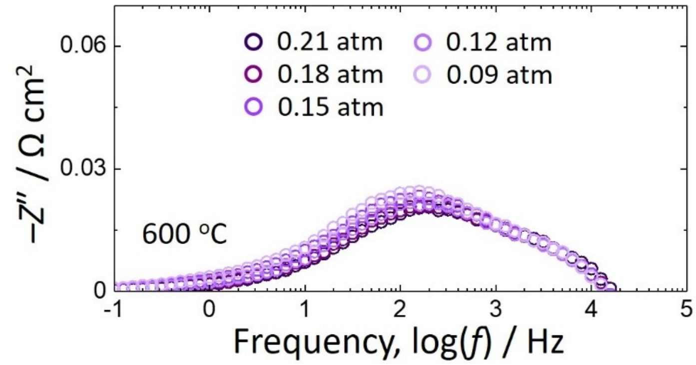

Figure S4. Bode plots of 600 ^{o}C EIS data for the STFC–LSGM electrode (~4.2 vol% STFC and ~8.5 μm thickness) symmetric cell with pO_2 varying from 0.09 to 0.21 atm.

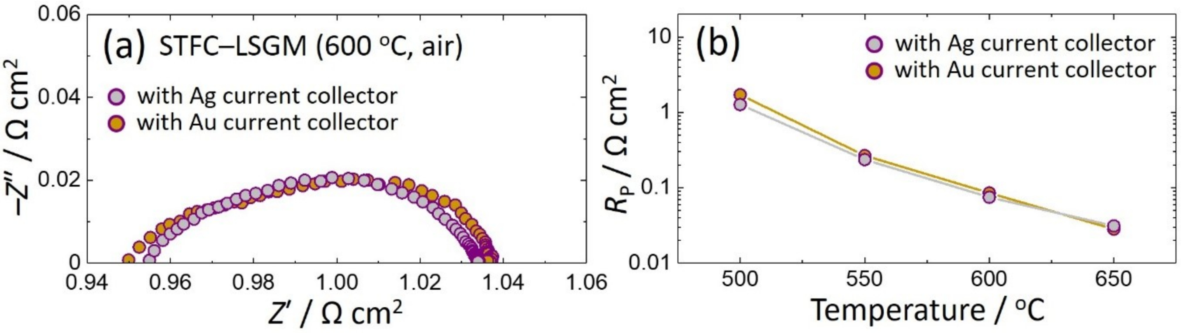

Figure S5. (a) Impedance Nyquist plots from the STFC–LSGM electrode symmetric cells with Ag and Au current collectors in air at 600 °C and (b) their R_P values versus temperature (500–650 °C).

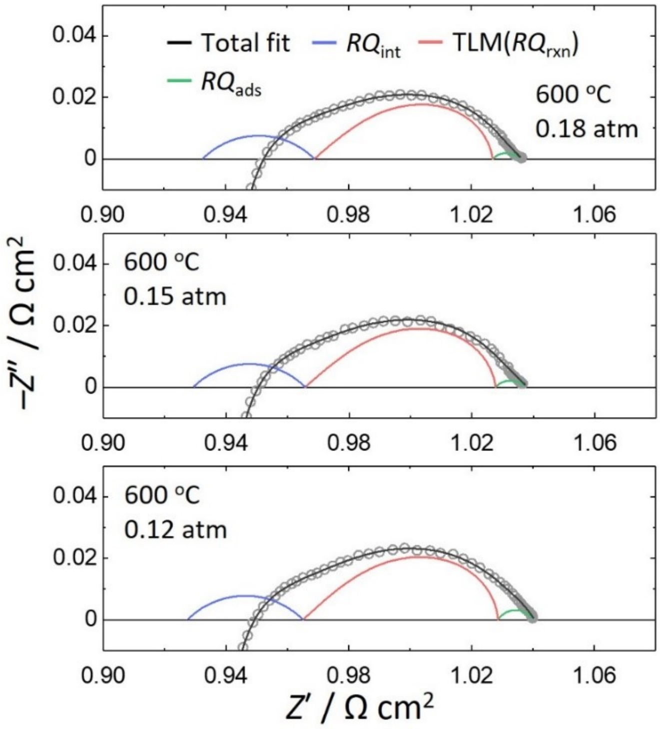

Figure S6. Nyquist plots of ECM fits to 600 °C EIS data for the STFC (~4.2 vol%)–LSGM electrode symmetric cell at pO_2 of 0.12, 0.15 and 0.18 atm.

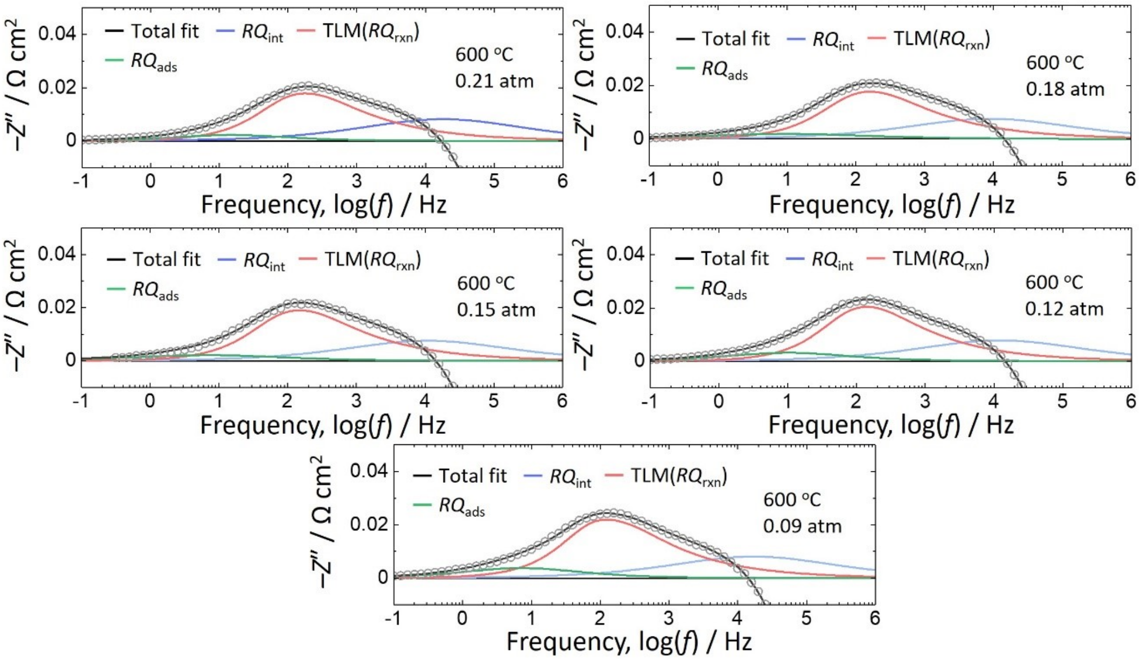

Figure S7. Bode plots of ECM fits to 600 °C EIS data for the STFC (~4.2 vol%)–LSGM electrode symmetric cell at pO_2 of 0.09–0.21 atm.

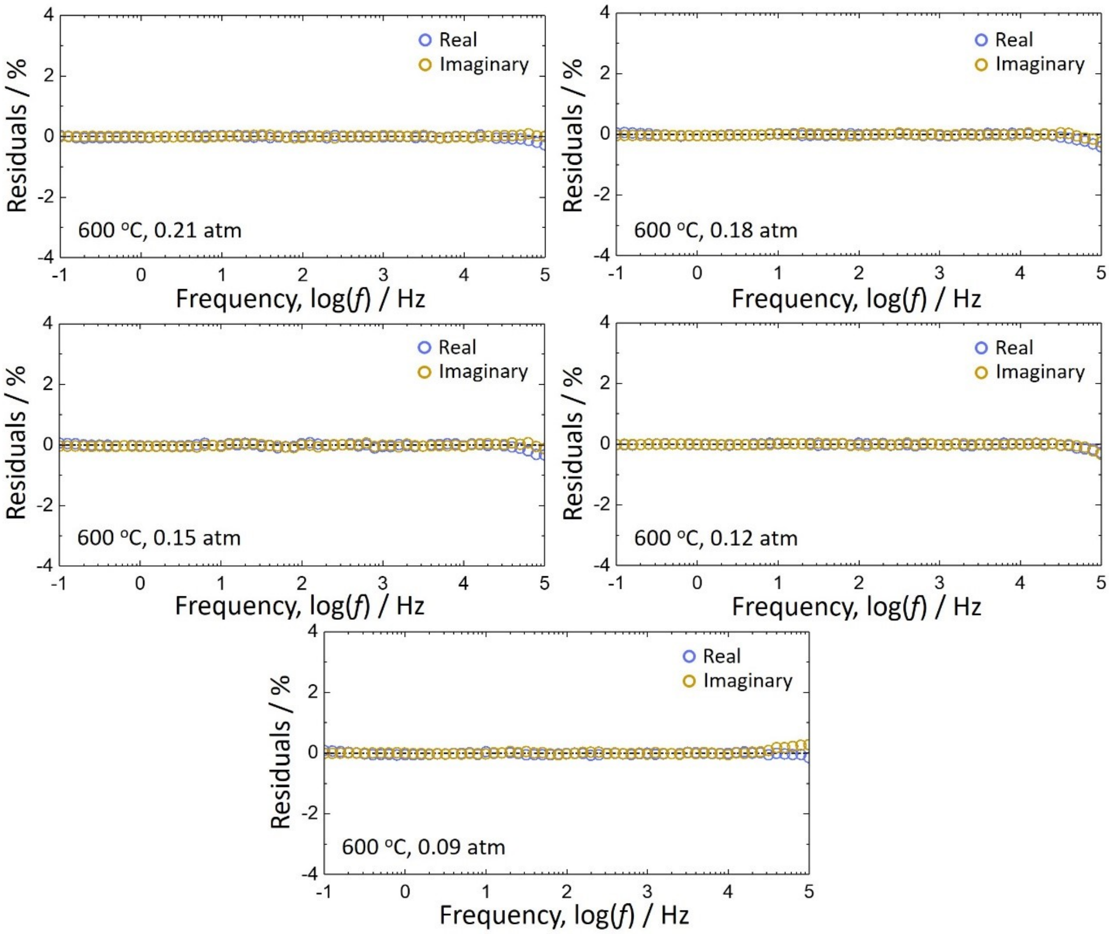

Figure S8. Relative residuals between the EIS data and the fits for the STFC (~4.2 vol%)–LSGM electrode symmetric cell measured at 600 ^{o}C with pO_2 varying from 0.09 to 0.21 atm, confirming the good fitting.

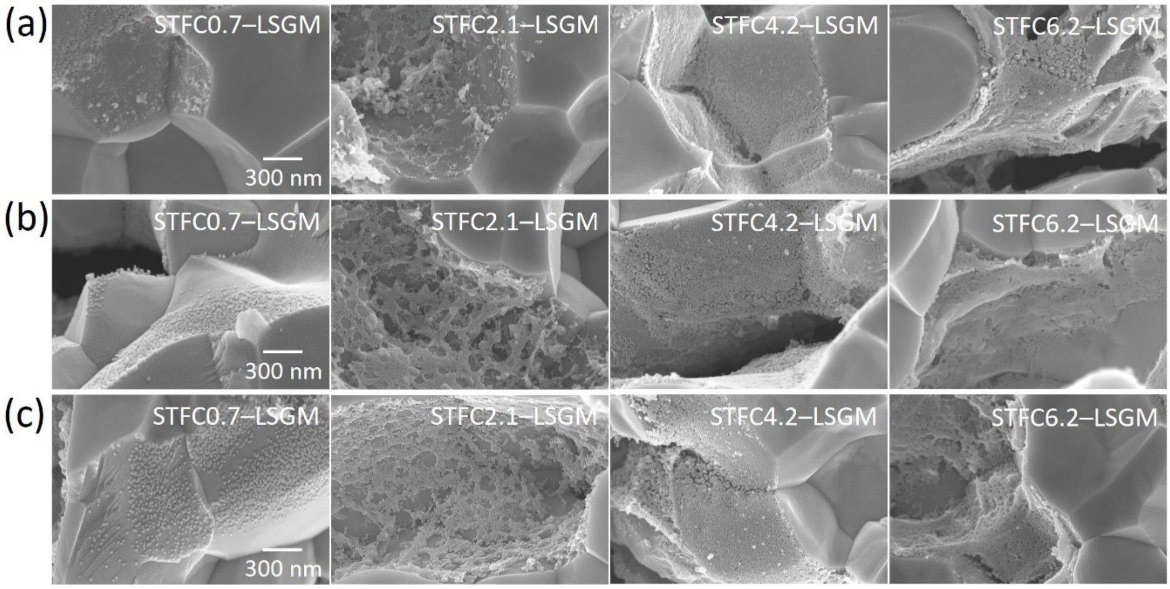

Figure S9. Fracture cross-sectional SEM images of STFC*x*–LSGM electrodes (*x* = ~0.7, ~2.1, ~4.2, and ~6.2 vol%), taken from three different regions of each electrode.

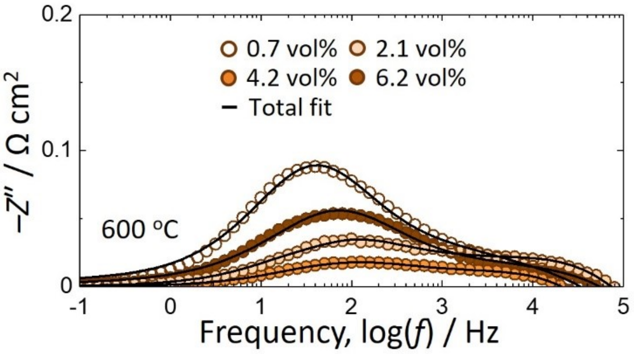

Figure S10. Bode plots of EIS data for the STFC*x*–LSGM electrode symmetric cells measured at 600 °C in air (*x* = ~0.7, ~2.1, ~4.2, and ~6.2 vol%), along with the best fits.

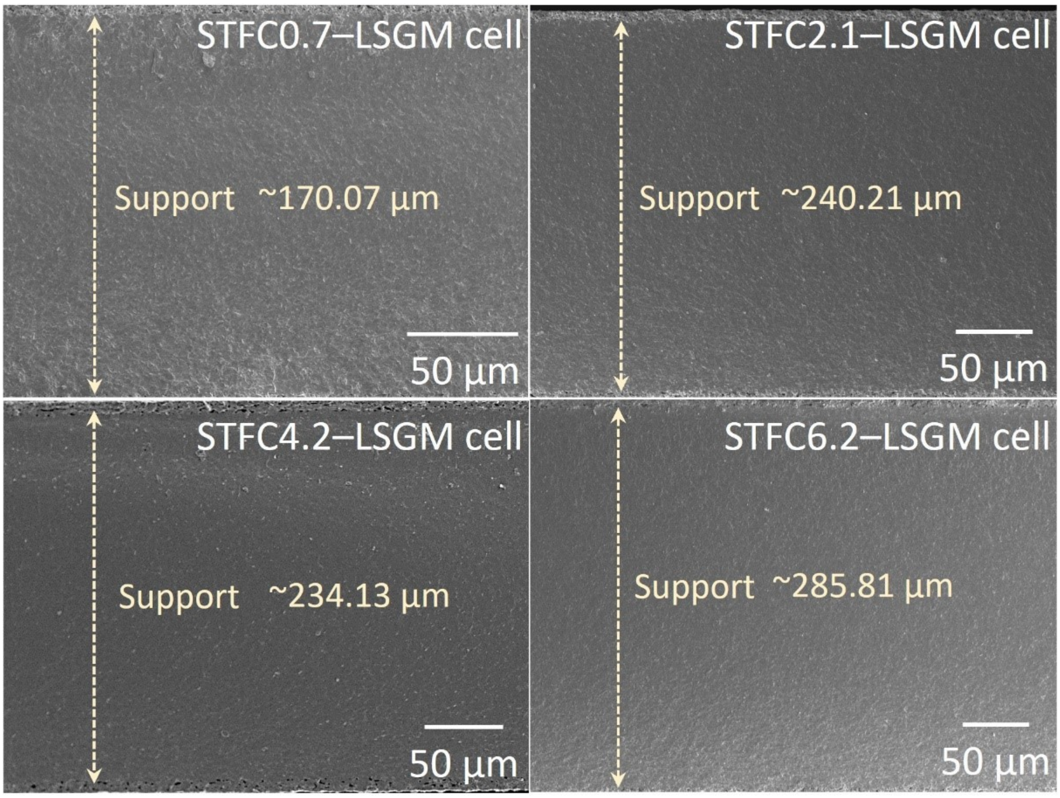

Figure S11. Fracture cross-sectional SEM images of the electrolyte supports for STFC*x*–LSGM electrode symmetric cells (*x* = ~0.7, ~2.1, ~4.2, and ~6.2 vol%).

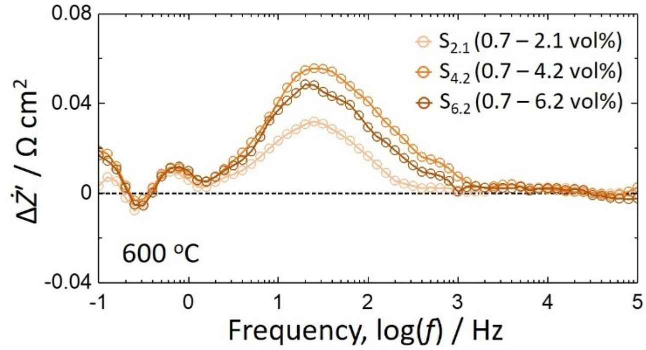

Figure S12. $\Delta\dot{Z}'$ spectra obtained from the 600 ^{o}C EIS data of STFC0.7–LSGM electrode symmetric cell, showing the changes induced by increasing the STFC fraction to ~2.1, ~4.2, and ~6.2 vol%. The spectrum S_x is obtained from the difference between the 600 ^{o}C EIS data of STFC*x*–LSGM (*x* = ~2.1, ~4.2, and ~6.2) and STFC0.7–LSGM.

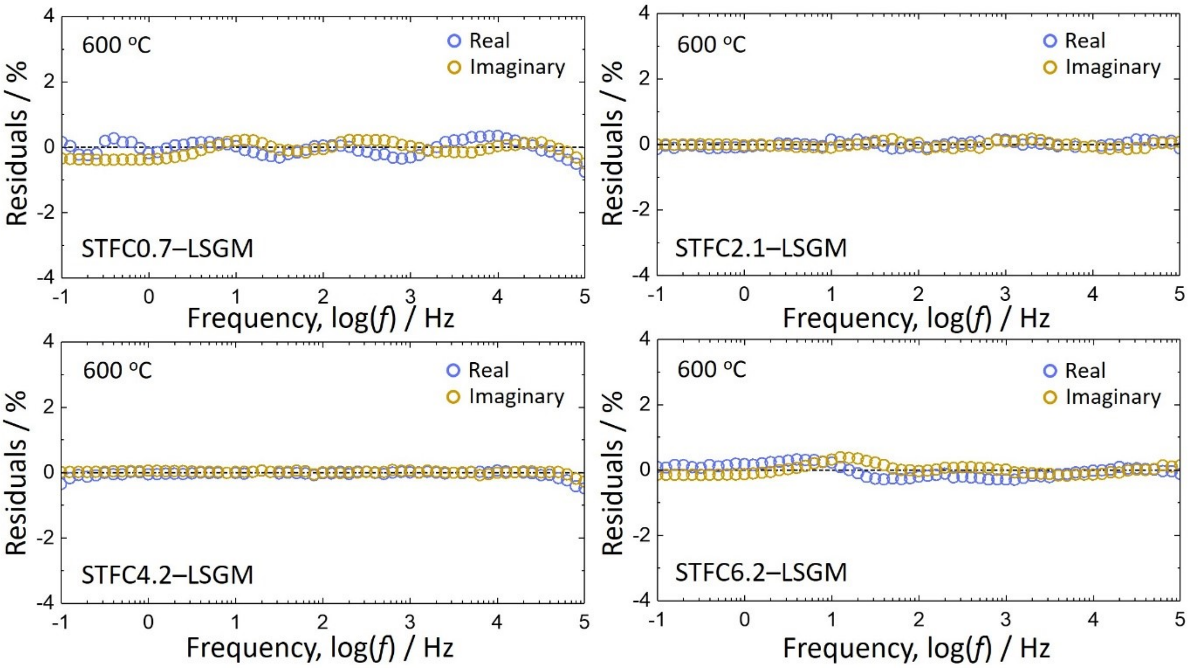

Figure S13. Relative residuals between the EIS data and the fits for the STFC*x*–LSGM electrode symmetric cells measured at 600 °C in air (*x* = ~0.7, ~2.1, ~4.2, and ~6.2 vol%), confirming the good fitting.

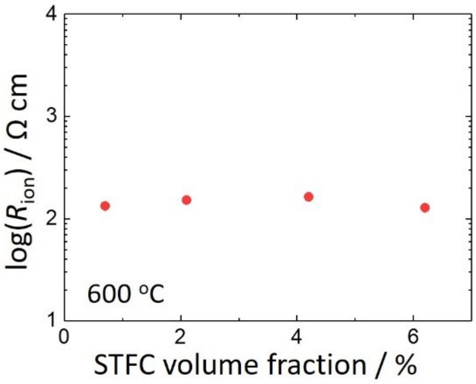

Figure S14. R_{ion} values for the STFCx–LSGM electrode symmetric cells at 600 °C (x = ~0.7, ~2.1, ~4.2, and ~6.2 vol%).

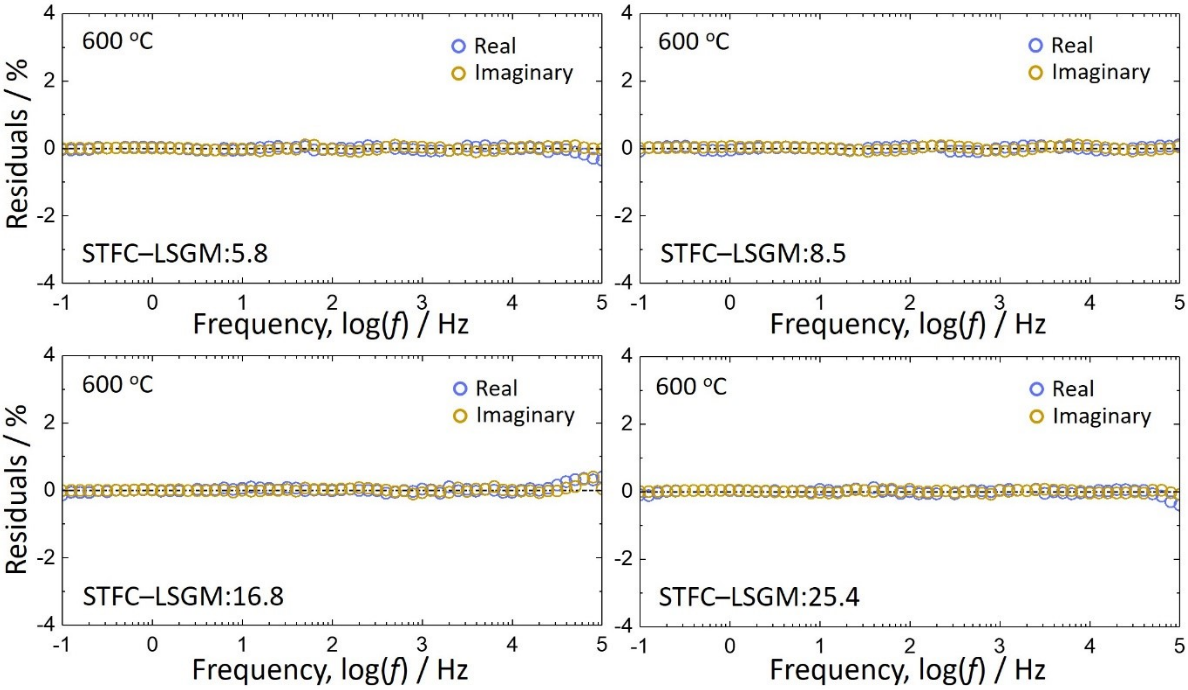

Figure S15. Relative residuals between the EIS data and the fits for the STFC–LSGM:*t* electrode symmetric cells measured at 600 °C in air (*t* = ~5.9, ~8.5, ~16.8, and ~25.4 μm), confirming the good fitting.

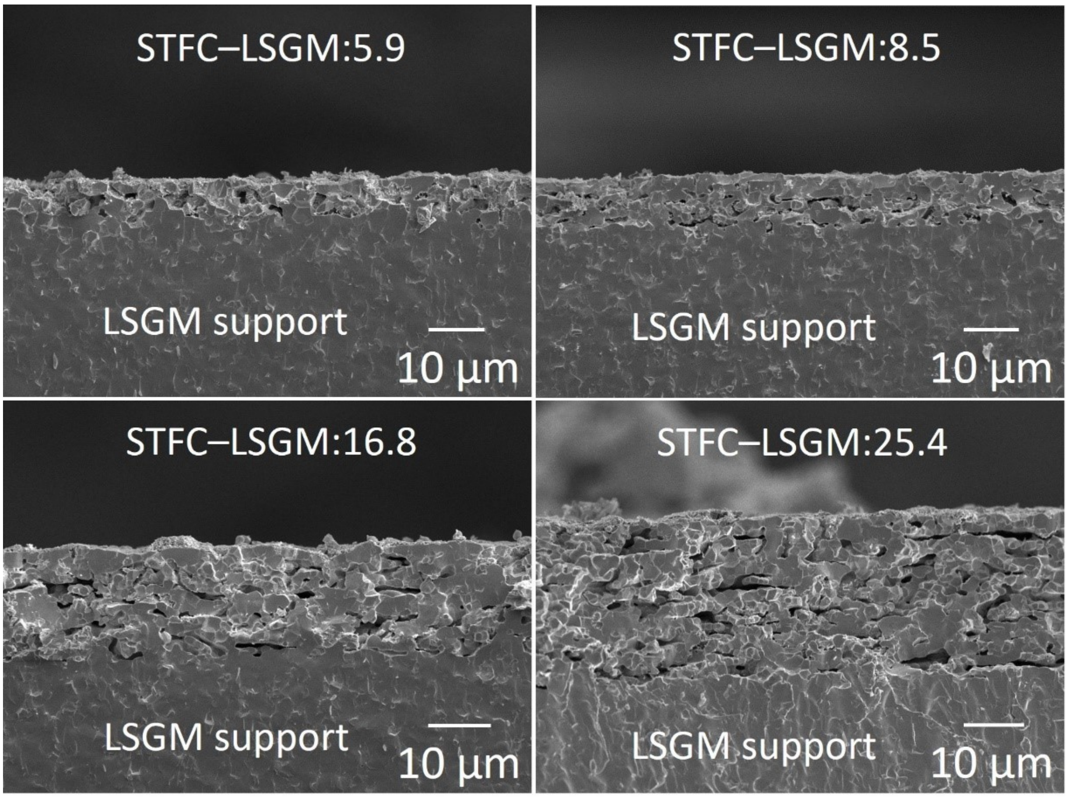

Figure S16. Cross-sectional SEM images of the tested STFC–LSGM:*t* electrode symmetric cells (t = ~5.9, ~8.5, ~16.8, and ~25.4 μm)

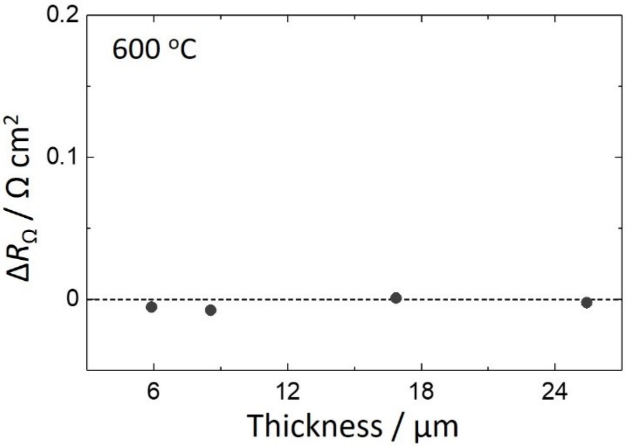

Figure S17. ΔR_{Ω} for the STFC–LSGM:t electrode symmetric cells at 600 °C (t = ~5.9, ~8.5, ~16.8, and ~25.4 μm).

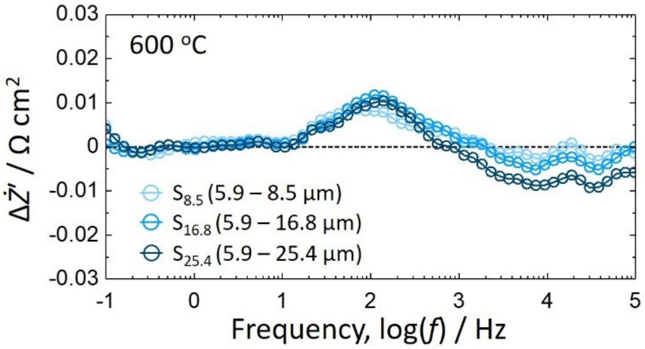

Figure S18. $\Delta\dot{Z}'$ spectra obtained from the 600 °C EIS data of STFC–LSGM:5.9 cell, showing the response changes induced by increasing the electrode thickness to ~8.5, ~16.8, and ~25.4 μm. The spectrum S_x is obtained from the difference between the 600 °C EIS data of STFC–LSGM:*t* (*t* = ~8.5, ~16.8, and ~25.4) and STFC–LSGM:5.9.

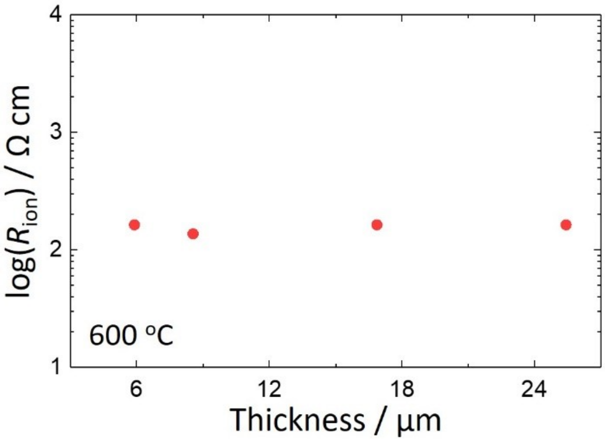

Figure S19. R_{ion} values for the STFC–LSGM:*t* electrode symmetric cells at 600 °C (*t* = ~5.9, ~8.5, ~16.8, and ~25.4 µm)

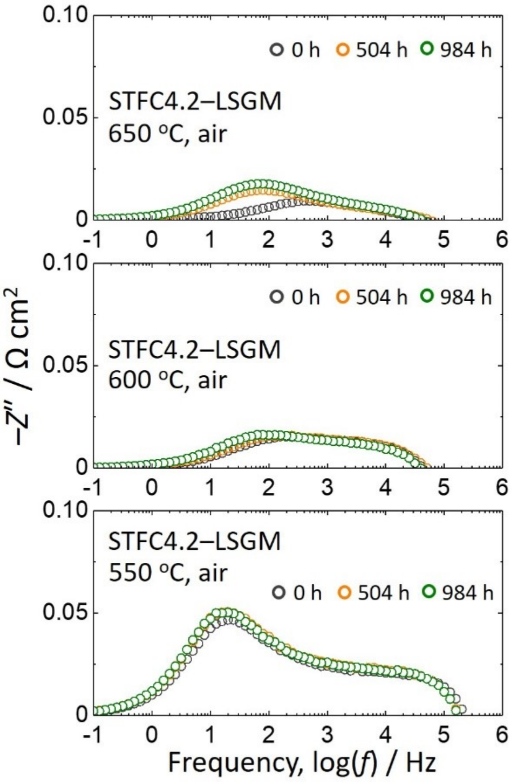

Figure S20. Bode plots of impedance spectra for STFC4.2–LSGM symmetric cells at 0, 504, and 984 h during stability tests at 550 , 600, and 650 °C in air.

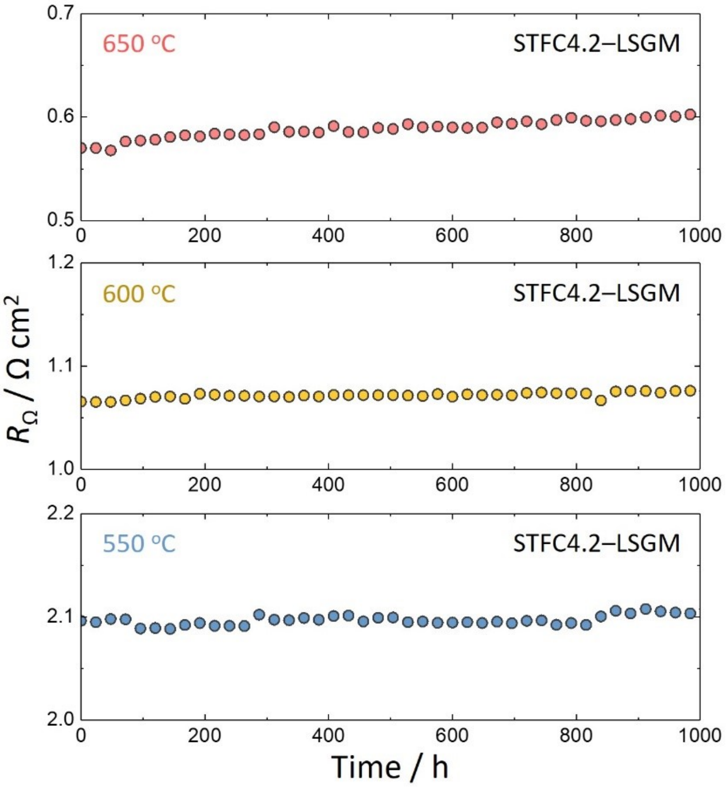

Figure S21. Evolution of R_Ω over time for the STFC4.2–LSGM electrode symmetric cells at 550, 600, 650 °C.

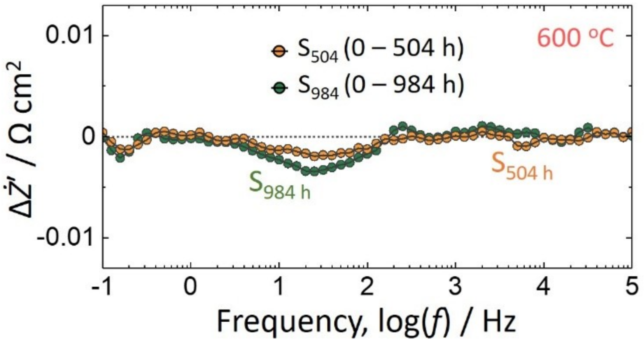

Figure S22. $\Delta\grave{Z}'$ spectra obtained from the 600 °C EIS data of STFC4.2–LSGM cell, showing the changes in response over time at 504 and 984 h after the initial measurement.

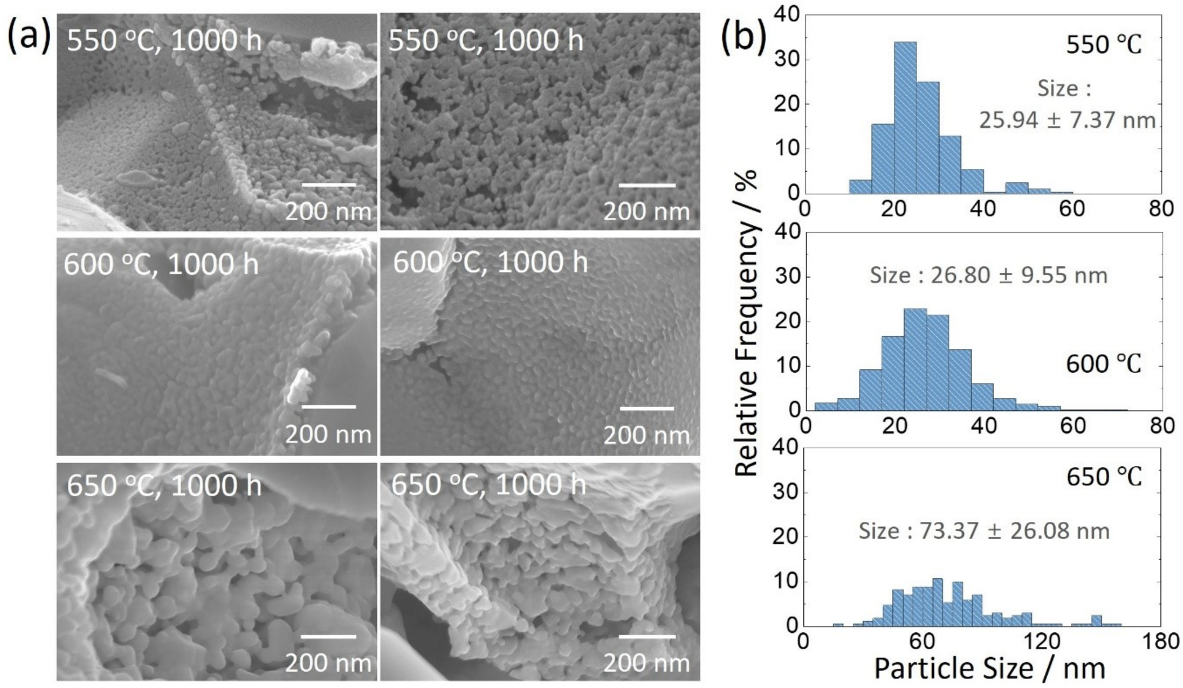

Figure S23. (a) High-magnification SEM images of the fracture cross-sections of STFC4.2–LSGM electrodes, taken from two different regions for each electrode, after 1000 h of testing at 550, 600, and 650 °C. (b) STFC particle size distribution analysis results for the stability-tested STFC4.2–LSGM electrodes.

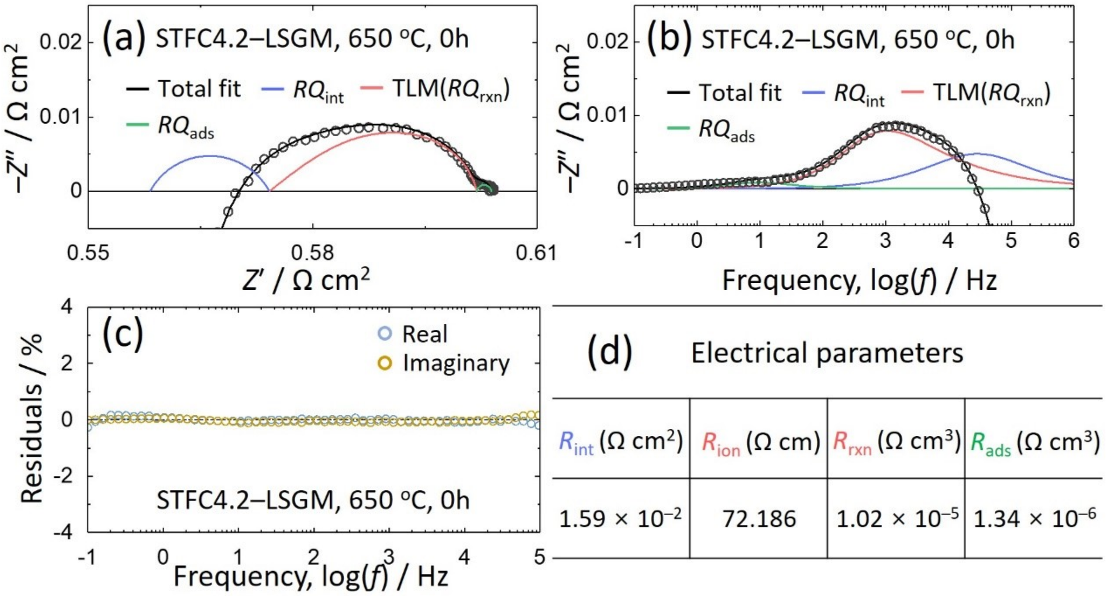

R_{int} (Ω cm^2)	R_{ion} (Ω cm)	R_{rxn} (Ω cm^3)	R_{ads} (Ω cm^3)
1.59×10^{-2}	72.186	1.02×10^{-5}	1.34×10^{-6}

Figure S24. (a) Nyquist and (b) Bode plots of ECM fits to 650 °C EIS data for the STFC4.2–LSGM electrode symmetric cell. (c) Relative residuals between the EIS data and the fits, confirming the good fitting. (d) Fitted values of R_{int}, R_{ion}, R_{rxn}, and R_{ads}.

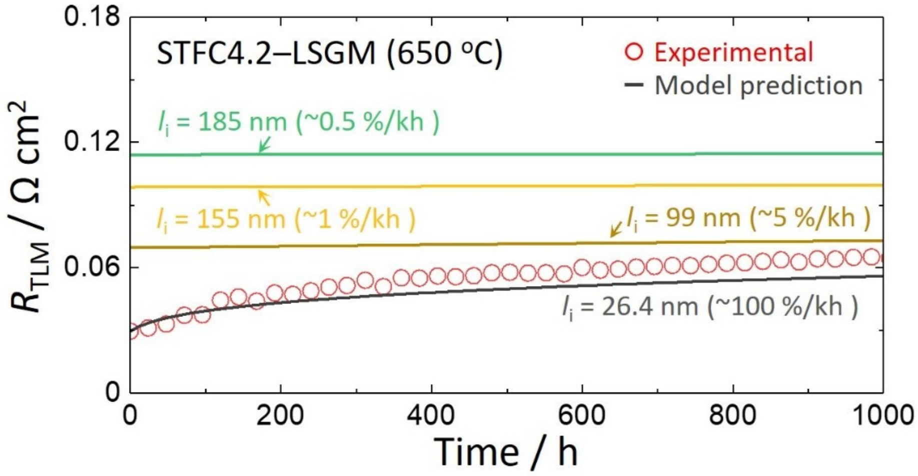

Figure S25. Predicted R_{TLM} as a function of time for STFC4.2–LSGM with initial particle sizes (l_i) of 26.4, 99, 155, and 185 nm, operated at 650 ^{o}C, along with the degradation rate. The experimental R_{TLM} is also shown for comparison.

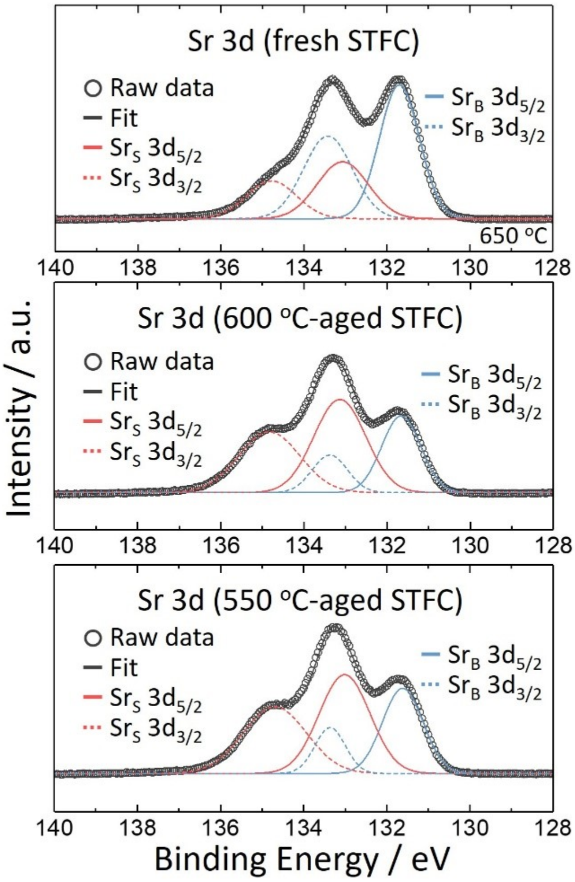

Figure S26. XPS spectra of Sr 3d level and the peak fittings for infiltration-solution-derived STFC powders: fresh *vs.* 1000 h-aged at 550 and 600 °C.

The XPS analysis was done for both fresh STFC powders and those aged for 1000 h at 550 and 600 °C, all derived from an infiltration solution. To detect any surface-segregated Sr species, peak fitting was performed on the XPS spectra of the Sr 3d level, as shown in Figure S26. The analysis, coupled with data reported in previous literature [1–3], suggests the presence of both bulk-bound Sr and surface-bound Sr, each possessing a double state – 3d$_{3/2}$ and 3d$_{5/2}$. The pair with lower binding energy, ~133.5 eV for 3d$_{3/2}$ and ~131.5 eV for 3d$_{5/2}$ can be assigned to Sr in the STFC perovskite oxide (Sr$_B$). On the other hand, the higher binding energy, ~135 eV for 3d$_{3/2}$ and ~133 eV for 3d$_{5/2}$ is attributed to surface Sr species, such as SrO, on the STFC surface (Sr$_S$).

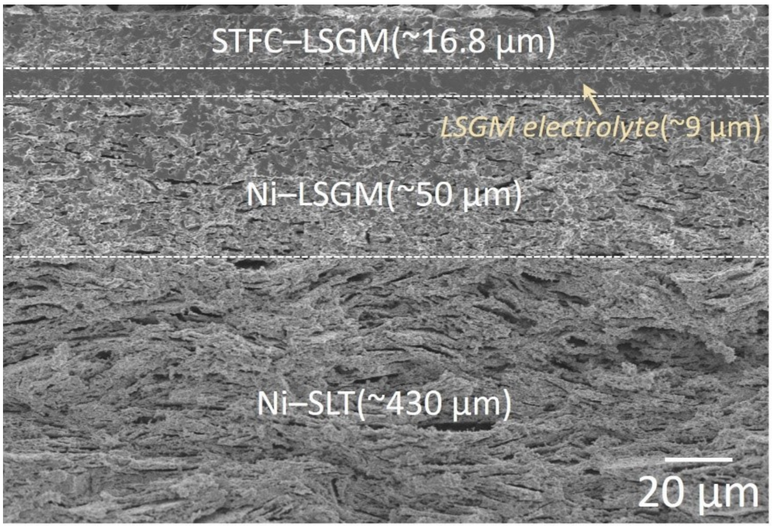

Figure S27. Fracture cross-sectional SEM image for the post-tested SLT-supported LSGM electrolyte full cell with the optimal oxygen electrode STFC4.2–LSGM:16.8.

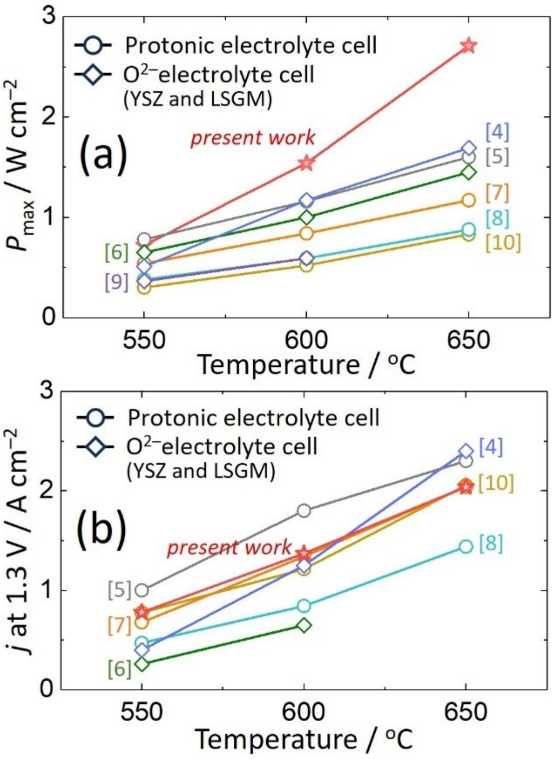

Figure S28. Comparison of the performance of the cell proposed herein with the performance of high-performance cells reported in the literature [4–10]: (a) Maximum fuel cell power density P_{max} and (b) steam electrolysis current density j at 1.3 V.

Figure S28 compares the performance of the present cell with literature data on oxygen and proton conducting electrolyte-based cells in the operating range between 550 and 650 °C [4–10], offering a preliminary perspective on the potential of the present cell type combined with infiltrated STFC–LSGM oxygen electrode. Note that this comparison focuses on YSZ and LSGM as representative O^{2-}-conducting electrolytes, known for their high ionic transference numbers and good thermodynamic efficiencies. The cell produced in this study exhibited exceptional fuel cell performance, comparable to the best-performing protonic electrolyte cells at 550 °C and surpassing them at higher temperatures. Notably, it achieved a peak power density of ~1.54 W cm^{-2} at 600 °C, exceeding the best reported value of ~1.17 W cm^{-2}. In the steam electrolysis mode, the cell exhibited a current density of ~1.37 A cm^{-2} at 1.3 V, competitive with the best-performing cells.

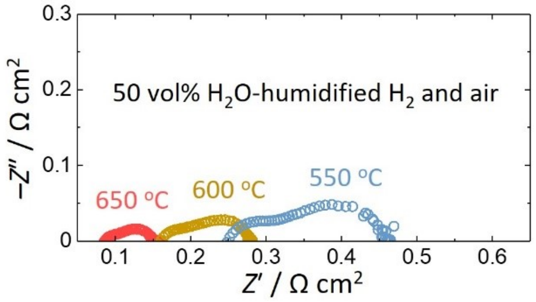

Figure S29. Nyquist plots of the stem electrolysis impedance spectra at 550, 600, and 650 ^{o}C.

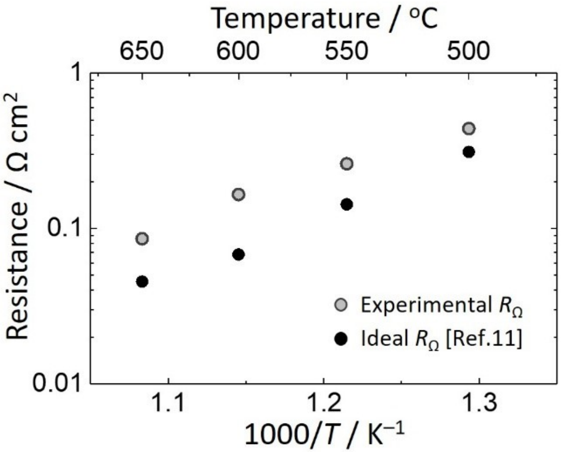

Figure S30. Comparison of the experimental and ideal ohmic resistances at different temperatures. The ideal values were estimated from the LSGM electrode thickness of ~9 μm and the conductivity reported in Ref.[11].

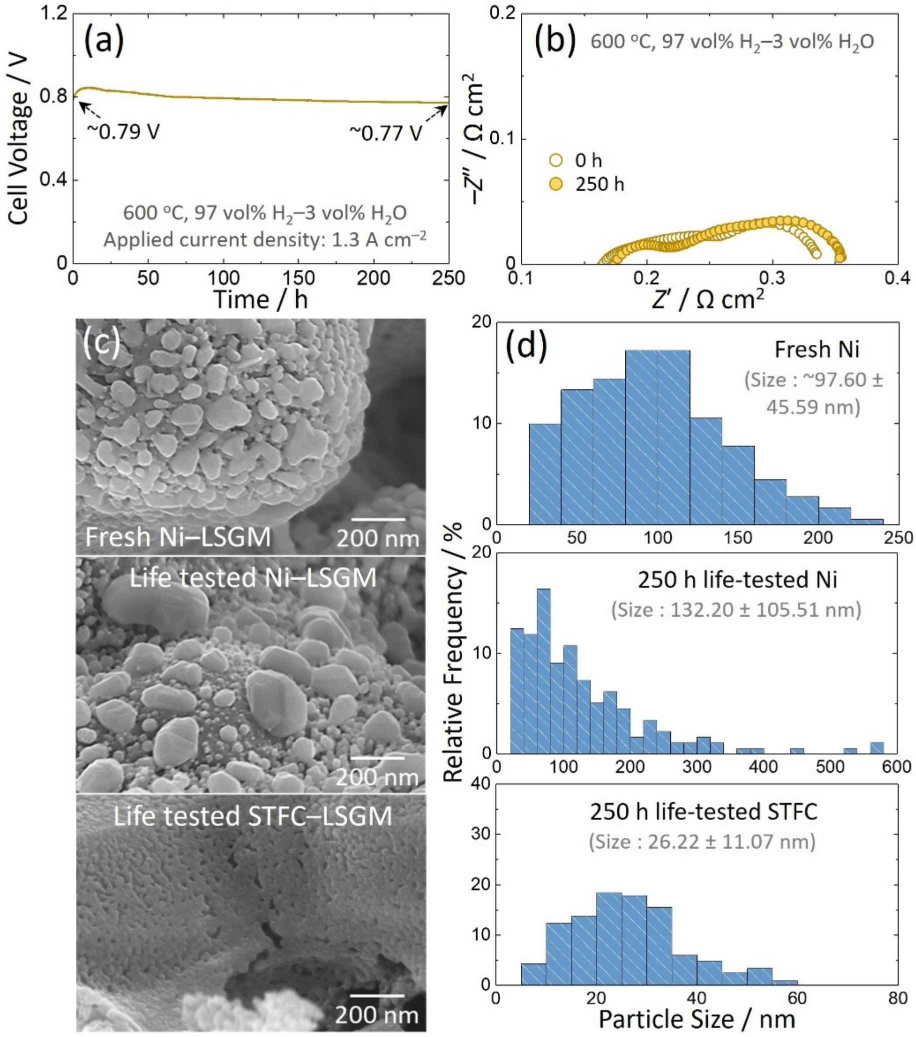

Figure S31. (a) Evolution of cell voltage over time during the fuel cell life test at a current density of 1.3 A cm^{-2} in 97 vol% H_2–3 vol% H_2O and air for the SLT-supported LSGM electrolyte cell with a Ni–LSGM fuel electrode and an STFC–LSGM oxygen electrode at 600 ^{o}C, where an Au current collector was employed. (b) Impedance Nyquist plots obtained at the beginning and end of the 250 h life test for the full cell under open-circuit voltage. (c) Magnified SEM images of fresh Ni–LSGM and life-tested Ni–LSGM and STFC–LSGM electrodes. (d) Particle size distribution analysis for fresh and life-tested Ni particles and life-tested STFC particles.

Figure S31(a) shows the voltage profile over time for the SLT-supported full cell with a Ni–LSGM fuel electrode and an STFC–LSGM oxygen electrode, tested in fuel cell mode in 3 vol% humidified H_2 and air at 600 ^{o}C. Under a current density of 1.3 A cm^{-2}, the cell voltage slightly increased from ~0.79 V during the first ~12 h but gradually decreased to ~0.77 V after 250 h. The impedance data in Figure S31(b) indicate increases in both R_{Ω} and R_{P} during the life test. Post-test SEM analysis (Figures S31 (c) and (d)) revealed significant Ni particle growth from ~97.6 nm to ~132.2 nm, while the STFC particle size remained relatively unchanged at ~26.2 nm, consistent with its pristine structure (Figure S3). Consequently, the observed cell degradation is likely attributed to the instability of the Ni nanostructure, aligning with the argument by Gao et al. regarding Ni coarsening at low temperatures [6]. A more detailed investigation is needed to fully understand the degradation mechanisms in such nanostructure-based cells.

References

[1] H.-G Seo, H.-S Kim, W.-C Jung, H.L. Tuller, *Appl. Catal. B: Environ. Energy,* 355 (2024) 124172.

[2] S.L. Zhang, H. Yang, B.-K. Park, C.X. Li, C.J. Li, S.A. Barnett, *J. Mater. Chem. A*, 7.3.7 (2019) 21447-21458.

[3] J.H. Zhang, C.X. Li, S.L. Zhang, *Int. J. Hydrogen Energy*, 79 (2024) 986-997.

[4] B.K. Park, R. Scipioni, Q. Zhang, D. Cox, P.W. Voorhees, S.A. Barnett, *J. Mater. Chem. A*, **2020**, 8, 11687-11694.

[5] Y. Zhou, W. Zhang, N. Kane, Z. Luo, K. Pei, K. Sasaki, Y. Choi, Y. Chen, D. Ding, M. Liu, *Adv. Funct. Mater.*, **2021**, 31, 2105386.

[6] Z. Gao, H. Wang, E. Miller, Q. Liu, D. Senn, S. Barnett, *ACS Appl. Mater. Interfaces*, **2017**, 9, 7115-7124.

[7] F. He, S. Liu, T. Wu, M. Yang, W. Li, G. Yang, F. Zhu, H. Zhang, K. Pei, Y. Chen, W. Zhou, Z. Shao, *Adv. Funct. Mater.*, **2022**, 32, 2206756.

[8] N. Wang, B. Yuan, F. Zheng, S. Mo, X. Zhang, L. Du, L. Xing, L. Meng, L. Zhao, Y. Aoki, C. Tang, S. Ye, *Adv. Funct. Mater.*, **2024**, 34, 2309855.

[9] D.Y. Jang, M. Kim, J.W. Kim, K. Bae, J.-w. Son, M.V.F. Schlupp, J.H. Shim, *J. Electrochem. Soc.*, **2017**, 164, F484.

[10] J.-S. Shin, H. Park, K. Park, M. Saqib, M. Jo, J.H. Kim, H.-T. Lim, M. Kim, J. Kim, J.-Y. Park, *J. Mater. Chem. A*, **2021**, 9, 607-621.

[11] R. Pelosato, C. Cristiani, G. Dotelli, S. Latorrata, R. Ruffo, L. Zampori, *J. Power Sources* **2010**, 195, 8116.